RSC Advances

PAPER

View Article Online
View Journal | View Issue

Cite this: *RSC Adv.*, 2022, **12**, 27072

Zinc vacancy modulated quaternary metallic oxynitride $GeZn_{1.7}ON_{1.8}$: as a high-performance anode for lithium-ion storage

Jinli Yao,[a] Fukun Ma,*[b] Yan-Jie Wang,*[b] Yinzhe Zuo [c] and Wei Yan*[c]

The development of alternative anode materials to achieve high lithium-ion storage performance is crucial for the next-generation lithium-ion batteries (LIBs). In this study, a new anode material, Zn-defected $GeZn_{1.7}ON_{1.8}$ ($GeZn_{1.7-x}ON_{1.8}$), was rationally designed and successfully synthesized by a simple ammoniation and acid etching method. The introduced zinc vacancy can increase the capacity by more than 100%, originating from the additional space for the lithium-ion insertion. This $GeZn_{1.7-x}ON_{1.8}$ particle anode delivers a high capacity (868 mA h g^{-1} at 0.1 A g^{-1} after 200 cycles) and ultralong cyclic stability (2000 cycles at 1.0 A g^{-1} with a maintained capacity of 458.6 mA h g^{-1}). Electrochemical kinetic analysis corroborates the enhanced pseudocapacitive contribution and lithium-ion reaction kinetics in the $GeZn_{1.7-x}ON_{1.8}$ particle anode. Furthermore, X-ray diffraction (XRD) and X-ray photoelectron spectroscopy (XPS) analyses at different electrochemical reaction states confirm the reversible intercalation lithium-ion storage mechanism of this $GeZn_{1.7-x}ON_{1.8}$ particle anode. This study offers a new vision toward designing high-performance quaternary metallic oxynitride-based materials for large-scale energy storage applications.

Received 25th July 2022
Accepted 3rd September 2022

DOI: 10.1039/d2ra04622a

rsc.li/rsc-advances

1. Introduction

Lithium-ion batteries (LIBs) have received particular attention as efficient energy storage and conversion devices, particularly for electric vehicles, portable powers, and stationary power plants.[1–3] However, the energy densities of LIBs are still not satisfactory for the long recharge mileages.[4,5] For further increasing the energy density of LIBs, both high capacity anode and cathode materials are required.[6,7] Regarding LIB anode materials, the commercially available graphite acting as the active LIB anode material seems to have insufficient capacity and high rate capability.[8,9] Besides, graphite anodes are susceptible to lithium metal dendrite formation, which can penetrate through the separator resulting in a short-circuit.[10,11] Therefore, efforts are still ongoing to explore alternative anode materials with high capacities and cyclic stabilities to support the continuous requirement for next-generation LIBs.[12] Among the different types of LIB anode materials, metal nitrides (*e.g.*, Ti–O–N,[13] Fe–O–N,[14] W–O–N,[15] and V–O–N[16]) have been recently studied as alternatives based on their advantages such as multiple electron transfers, negative redox voltages, and high theoretical capacities.[17] They operate *via* a conversion mechanism at the particle surfaces, with the reduction of the metal nitride to the metal, presumably with the formation of amorphous lithium nitride (Li_3N). Therefore, the irreversible crystalline-phase transformation will lead to low coulombic efficiencies, while pulverization will result in the loss of electrical contact for active materials and the repeated formation of the solid electrolyte interphase (SEI) layer. Nevertheless, the metal nitride-based anodes show sluggish charge transport and extreme volumetric variation during the electrochemical reaction.[18] Furthermore, the undesired side reaction can give rise to inferior coulombic efficiency with the "dead lithium".[19,20] In order to realize fast charge transport efficiency, high capacity, and cyclic stability, new material structures with favorable electrical conductivity and structural stability need to be developed.[21] As reported, metallic oxynitrides, a kind of hybrid anionic materials, have been lately explored as potential anode-active materials for higher energy/power densities of LIBs because of their excellent chemical/structural stability.[22,23]

In metallic oxynitrides, as the electronegativity of N is less than that of O, the introduction of N 2p orbitals can decrease the position of the maximum valence bands (VBs) and enhance the electron conduction efficiency.[24] For example, as a typical quaternary crystal with a hexagonal wurtzite structure, $GeZn_{1.7}ON_{1.8}$ possesses low conversion potential and high

[a]*Department of Research and Development, Meijin Energy Ltd, Beijing 100052, China. E-mail: mafukun666@126.com; wyj@dgut.edu.cn*

[b]*New Energy and Advanced Functional Materials Group, School of Materials Science and Engineering, Dongguan University of Technology, Dongguan 523808, Guangdong, China*

[c]*College of Materials Science and Engineering, Fuzhou University, Fuzhou 350108, China. E-mail: weiyan@fzu.edu.cn*

saturated electron mobility. The less electronegative N atom, when introduced, can result in the p-d repulsion between the Zn 3d and N 2p orbitals with enhanced electron transfer efficiency.[24] Consequently, $GeZn_{1.7}ON_{1.8}$ exhibits high conductivity and fast ionic diffusion than those of traditional metal nitrides, and its excellent structural and chemical stability also favor its usage in violent electrochemical reaction environments.[25] Therefore, $GeZn_{1.7}ON_{1.8}$ is considered to be the promising alternative anode-active material with excellent structural stability in electrochemical reactions for the lithium-ion storage, which is even superior to the conventional metal nitride-based anode materials. However, when it comes to practical applications, issues such as unsatisfied lithium-ion transport kinetics and cycling capacity have been identified, which resulted from their insufficient conductance and active sites. Furthermore, the SEI film grown during the electrochemical reaction could easily lead to an inferior coulombic efficiency and dead lithium near the anode surface. Based on previous reports, morphological and structural design strategies could be adopted to improve the charge transport efficiency, capacities and cyclic stability of the anode-active materials for higher electrochemical performance.[26] Unfortunately, although some progress has been made, the ion diffusion efficiency and conductance of the $GeZn_{1.7}ON_{1.8}$-based anode could still not be intrinsically improved, and its rate capability and cycling capacity are still unsatisfactory and need to be further improved. To address these issues and improve lithium-ion storage performance, defect engineering has been proposed to be an effective method to regulate the electron density and ion diffusion efficiency of the anode-active materials for higher energy/power densities.[27,28] With respect to this, zinc vacancies have been identified to be able to provide a larger interface for lithium-ion and electron insertion/extraction, activating more reactive sites and extending faster transport paths, thus greatly improving the electrochemical performance of the materials.[29] However, the prepared Zn-defected $GeZn_{1.7}ON_{1.8}$ particle anodes for obtaining the best electrochemical performance have not been optimized thus far.

In this study, $GeZn_{1.7-x}ON_{1.8}$ particles were successfully synthesized using ammoniation and the acid etching method. XRD, EDS, EPR and XPS results further confirmed the successful synthesis of $GeZn_{1.7-x}ON_{1.8}$ particles. The improvement in lithium-ion storage performance using these materials as anodes was validated by electrochemical measurements. Compared with the pristine $GeZn_{1.7}ON_{1.8}$ particle anode, the $GeZn_{1.7-x}ON_{1.8}$ particle anode exhibits a higher superior reversible capacity, rate capability, and ion diffusion coefficient as indicated by the systematic electrochemical measurements and kinetic analysis. The XRD and XPS analyses were used to reveal the reversible lithium-ion storage mechanism for fundamental understanding. As a result, a $GeZn_{1.7-x}ON_{1.8}$ particle anode shows a reversible specific capacity of 878.6 mA h g^{-1} after 200 cycles at 0.1 A g^{-1}. The defect engineering employed in this study is significant for the rational regulation of charge transfer and high-performance lithium-ion storage of anode materials.

2. Experimental section

2.1. Material synthesis

For the material synthesis as shown in Fig. 1, GeO_2 and ZnO (Zn : Ge = 1 : 1) powders were thoroughly ground and mixed in an agate mortar and then placed in a porcelain boat in the middle of a horizontal high-temperature tube furnace. The quartz reactor was pumped (≤1 mTorr) and then purged with nitrogen (N_2). Nitrogen was used as a protective atmosphere to prevent the oxidation of the raw material at high temperatures. The nicely mixed GeO_2 and ZnO were further treated at 850 °C in NH_3 atmosphere for 2 h. After cooling down to room temperature, $GeZn_{1.7}ON_{1.8}$ particles were obtained on porcelain boats. $GeZn_{1.7-x}ON_{1.8}$ particles were obtained *via* the corrosion of $GeZn_{1+x}ON$ in 2.0 mol L^{-1} hydrochloric acid. After the corrosion process, the obtained $GeZn_{1.7-x}ON_{1.8}$ particles were collected by washing several times with ethanol and ultrapure water.

2.2. Material characterizations

The morphology of the samples was examined using scanning electron microscopy (SEM, Hitachi S-4800) and a transmission electron microscopy (TEM, Tecnai 20U dual microscope). The scanning of energy dispersive spectroscopy (EDS) elements was performed using the same instrument equipped with a detector (7593-H, Horiba). X-ray diffraction (XRD) patterns were obtained using a diffractometer with Cu-Kα radiation (λ = 0.15443 nm, X'pert Pro MPD). X-ray photoelectron spectroscopy (XPS) was inspected using a Thermo ESCALAB 250.

2.3. Battery preparation and electrochemical measurements

The electrochemical behavior of pristine $GeZn_{1.7}ON_{1.8}$ particles and $GeZn_{1.7-x}ON_{1.8}$ particles was studied by assembling CR2016 type coin-shaped batteries. In the anode preparation process, 80 wt% of active material, 10 wt% of conductive carbon (Ketjen black) and 10 wt% of polyvinylidene fluoride (PVDF) were mixed in *N*-methyl-2-pyrrolidone as a binder, and then the fully mixed active material was adhered to the copper foil and then dried at 80 °C under vacuum overnight prior to use. The active material had an average loading density of about 1.5 mg and a diameter of 16 mm. Lithium metal was used as the counter and reference electrodes. The electrolyte solution was $LiPF_6$ (1 M) in vinyl carbonate/dimethyl carbonate/diethyl carbonate (1 : 1 : 1 vol%). Cyclic voltammetry (CV) and electrochemical impedance spectroscopy (EIS) were conducted using a CHI660D electrochemical workstation. The galvanostatic charge/discharge curves were recorded using a Neware CT-3008W battery system.

3. Results and discussion

As shown in Fig. 2a–c, the $GeZn_{1.7-x}ON_{1.8}$ particles agglomerated after calcination in an ammonia atmosphere at high temperatures. The low-magnification TEM image (Fig. 2d) displays homogeneous $GeZn_{1.7-x}ON_{1.8}$ particles prepared by the ammoniation and acid etching method, and the average size of $GeZn_{1.7-x}ON_{1.8}$ particles is ~200 nm. The regular atomic

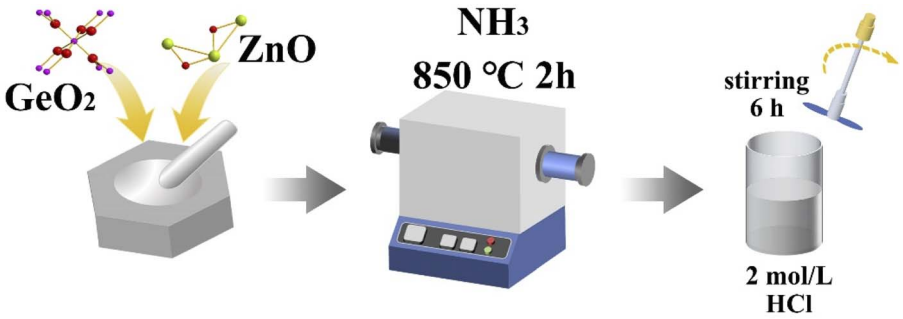

Fig. 1 Schematic of the preparation process of $GeZn_{1.7-x}ON_{1.8}$ particles.

arrangement can be observed in the HRTEM image (Fig. 2e), which shows the well-crystallized structure of $GeZn_{1.7-x}ON_{1.8}$ particles. The high-resolution lattice stripes with an interplanar distance of 0.27 nm can be indexed to the (100) crystal plane of $GeZn_{1.7}ON_{1.8}$ (Fig. 2f),[30] and it is expected that the high crystallinity of the $GeZn_{1.7-x}ON_{1.8}$ particles is important for the high-rate performance energy storage device. The SEM image and the corresponding EDS elemental mapping results (Fig. 2g–k) demonstrate the uniform distribution of Ge, Zn, O, and N elements in $GeZn_{1.7-x}ON_{1.8}$ particles, indicating that $GeZn_{1.7-x}ON_{1.8}$ particles were successfully synthesized.

The crystallographic structure of $GeZn_{1.7-x}ON_{1.8}$ particles was further analyzed by the X-ray diffraction (XRD) technique. As shown in Fig. 3a, the $GeZn_{1.7-x}ON_{1.8}$ particles maintain the hexagonal wurtzite structure, which can be easily indexed with $GeZn_{1.7}ON_{1.8}$ (PDF#24-1443). After acid etching, the $GeZn_{1.7-x}ON_{1.8}$ particles maintain the same lattice structure as the pristine $GeZn_{1.7}ON_{1.8}$ particles with a slight low-angle shift of the (101) peak, indicating the expanded crystal plane spacing after acid etching.[31] The high-resolution XPS spectra of Zn 2p (Fig. 3b) could be deconvoluted into two distinct peaks at 1022.5 eV and 1045.7 eV, depending on the location of Zn $2p_{1/2}$ and Zn $2p_{2/3}$, respectively.[32] The binding energy difference

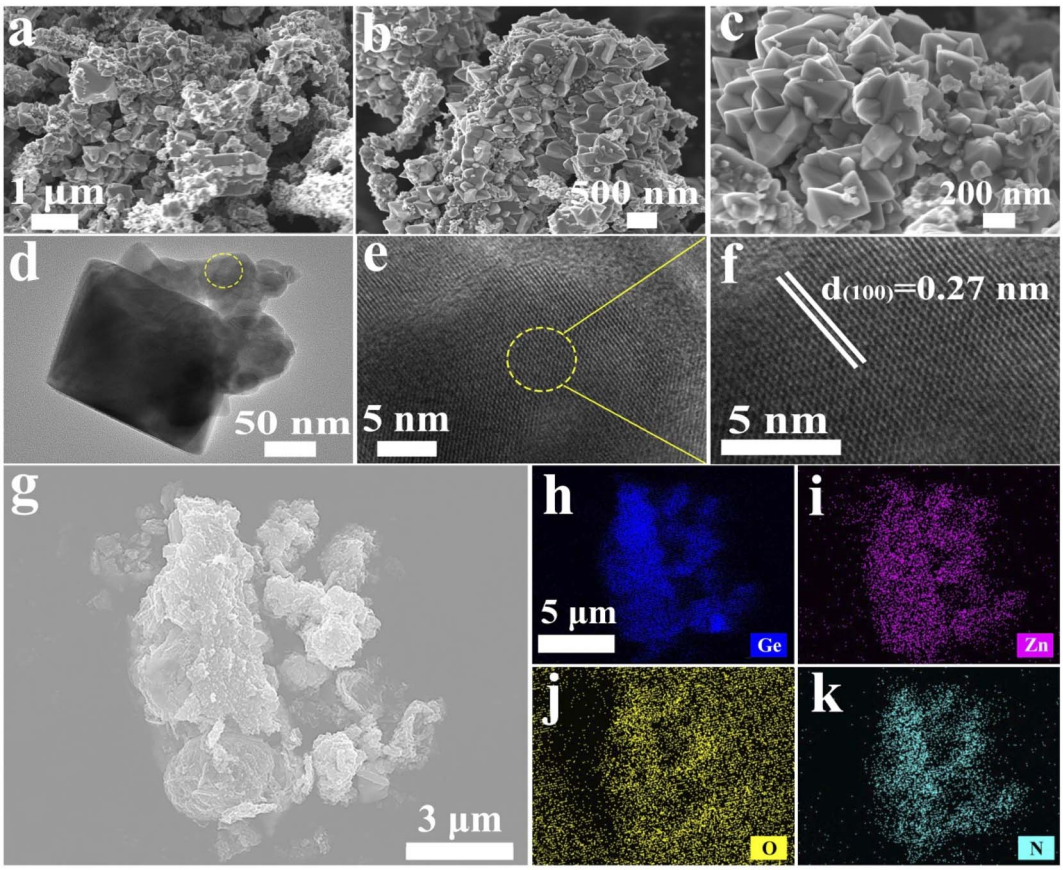

Fig. 2 (a) Low-magnification SEM image, (b) and (c) high-magnification SEM images, (d) TEM image, and (e) and (f) HRTEM images of Zn-defected $GeZn_{1.7}ON_{1.8}$ particles. (g)–(k) SEM image and the corresponding EDS elemental mapping of Zn-defected $GeZn_{1.7}ON_{1.8}$ particles.

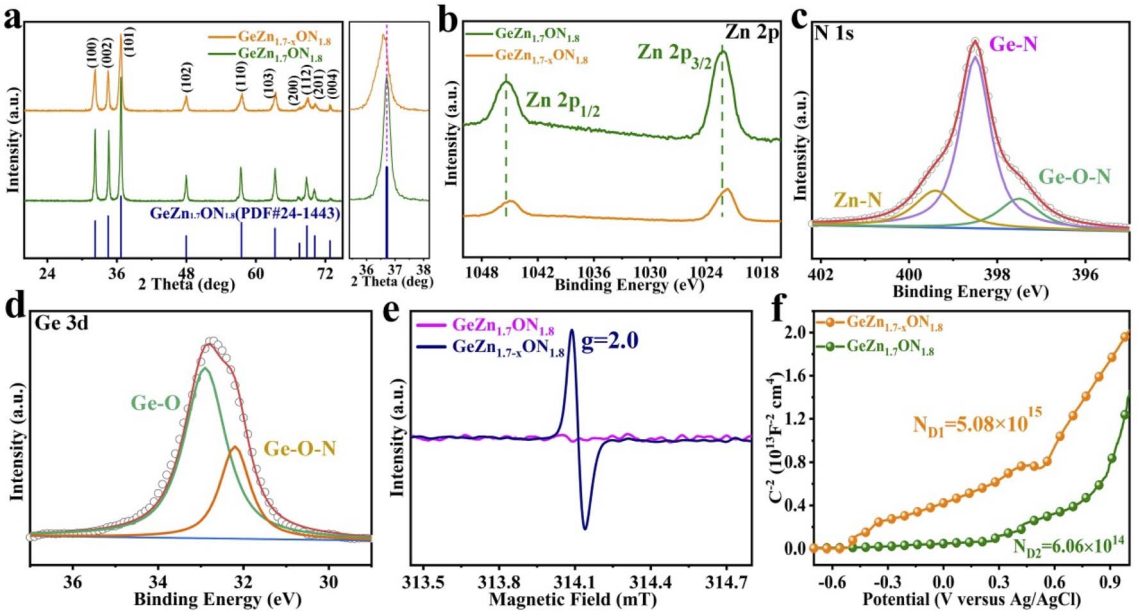

Fig. 3 (a) XRD patterns of $GeZn_{1.7-x}ON_{1.8}$ and $GeZn_{1.7}ON_{1.8}$ particles, the main diffraction peak is enlarged between 35.5° and 38.2°. The corresponding high-resolution XPS spectra for (b) Zn 2p, (c) N 1s, and (d) Ge 3d of $GeZn_{1.7-x}ON_{1.8}$ particles. (e) EPR spectra and (f) Mott–Schottky plots of $GeZn_{1.7-x}ON_{1.8}$ and $GeZn_{1.7}ON_{1.8}$ particles.

(23.1 eV) between Zn $2p_{1/2}$ and Zn $2p_{2/3}$ shows the Zn^{2+} oxidation state in the $GeZn_{1.7-x}ON_{1.8}$ particles.[33] It can be clearly observed that the Zn 2p binding energy of $GeZn_{1.7-x}ON_{1.8}$ particles shifts to a lower binding energy compared to that of pristine $GeZn_{1.7}ON_{1.8}$ particles, which is attributed to the change in the surface electron density in the presence of defects states.[34] It has been reported that the change in the binding energy could be related to the change in the surface electron density, while zinc vacancies increase the surface electron density.[35] In Fig. 3c, the high-resolution XPS spectra of N 1s show the Ge–O–N, Ge–N, and Zn–N bonds at 397.6, 398.3, and 399.6 eV, respectively.[36] As reported, the Ge–O–N bond can improve the reaction kinetics and lithium-ion storage performance of the $GeZn_{1.7-x}ON_{1.8}$ particle anode.[37] As shown in Fig. 3d, the high-resolution XPS spectra of Ge 3d show the Ge–O and Ge–O–N bonds at 32.8 and 32.2 eV, respectively.[38,39] The above-mentioned characterizations demonstrate that the $GeZn_{1.7-x}ON_{1.8}$ particles were successfully synthesized.

To obtain an in-depth understanding of the chemical environment and unravel Zn vacancies, the electron paramagnetic resonance (EPR) spectroscopy analysis was performed. As shown in Fig. 3e, no signal was observed in $GeZn_{1.7}ON_{1.8}$ particles, while a prominent signal ($g = 2.0$) appears at 314.1 mT in $GeZn_{1.7-x}ON_{1.8}$ particles, which clearly indicate that this material possesses numerous Zn vacancies.[40] Zinc vacancies can be considered to be the "electron acceptors", and the significant signal in $GeZn_{1.7-x}ON_{1.8}$ particles can be attributed to the spin resonance of the electrons captured by zinc vacancies.[35] Mott–Schottky plots were measured in 0.1 M Na_2SO_4 buffer at a frequency of 10 kHz in order to investigate the charge-carrier density changes of $GeZn_{1.7}ON_{1.8}$ and $GeZn_{1.7-x}ON_{1.8}$ particles. As shown in Fig. 3f, the positive slope in the linear region reveals the n-type semiconductor properties of $GeZn_{1.7}ON_{1.8}$ and $GeZn_{1.7-x}ON_{1.8}$ particles. The charge-carrier density (Nd) was calculated according to $N_D = (2/e_0\varepsilon\varepsilon_0)/[d(1/C^2)/dV]^{-1}$, where e_0 is the electron charge (1.6×10^{-19} C), ε is the dielectric constant, ε_0 is the permittivity of vacuum (8.85×10^{-12} F m^{-1}), and V is the applied potential.[41] The calculated carrier concentrations are 50.86×10^{14} and 6.06×10^{14} cm^{-3} for $GeZn_{1.7-x}ON_{1.8}$ and $GeZn_{1.7}ON_{1.8}$, respectively, indicating the improved electronic conductivity after the introduction of Zn vacancies. These results confirm the successful construction of $GeZn_{1.7-x}ON_{1.8}$ particles with the efficient electron transport, which is indispensable to activate the electrochemical response with a high-rate performance energy storage device.

The CV curves were first performed to gain a better understanding of the electrochemical reaction mechanism of the $GeZn_{1.7-x}ON_{1.8}$ particles at 0.1 mV s^{-1} from 0.01 to 3.0 V (*vs.* Li/Li^+). As shown in Fig. 4a, during the first discharge process, the irreversible broad peak at ~1.6 V could be attributed to the formation of the solid electrolyte interface (SEI) film.[42] The irreversible SEI peak disappears in the subsequent discharge process. The broaden peak centered at 0.5–0.8 V can be attributed to the reversible lithium-ion insertion with the formation of $Li_xGeZn_{1.7-x}ON_{1.8}$.[43] In the following charge process, the peaks at 1.1 and 2.0 V are ascribed to the lithium-ion desertion from the $GeZn_{1.7-x}ON_{1.8}$ anode.[44] The insertion/desertion peaks are stable in the second to fifth CV cycles, reflecting the reversible lithiation/delithiation mechanism of the $GeZn_{1.7-x}ON_{1.8}$ anode. In the subsequent cycles, the overlapped CV curves and the stable insertion/extraction peaks indicate the excellent stability of the discharge and charge processes. More importantly, the lithiation and delithiation peaks are entirely different from the reported metal-based anode.[45] Therefore, the

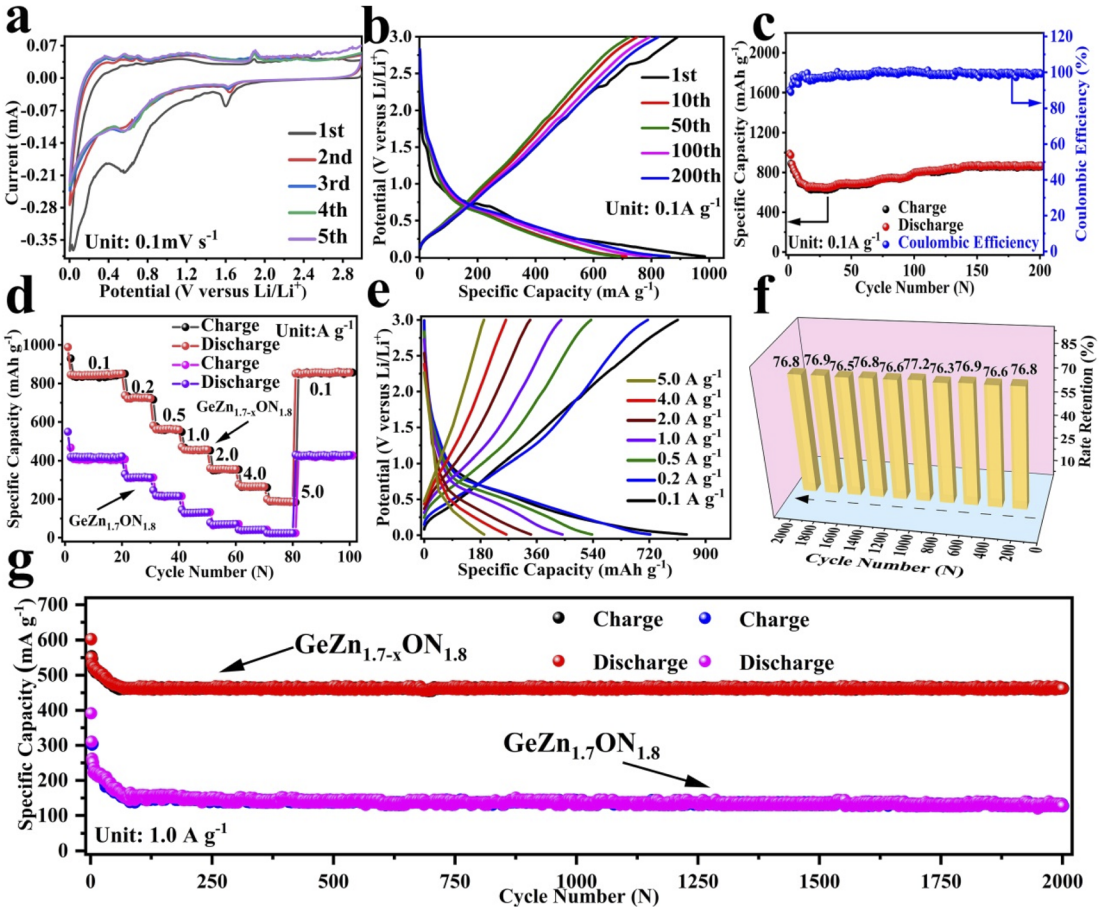

Fig. 4 Electrochemical properties of the $GeZn_{1.7-x}ON_{1.8}$ particle anode: (a) CVs at 0.1 mV s^{-1}. (b) Charge/discharge curves and (c) cycle property at 0.1 A g^{-1}. (d) Rate capabilities from 0.1 to 5.0 A g^{-1} and (e) the corresponding galvanostatic charge/discharge profiles from 0.1 to 5.0 A g^{-1}. (f) Long cycle retention histogram at 1.0 A g^{-1}. (g) Cycling property comparison at 1.0 A g^{-1}.

lithiation mechanism of the $GeZn_{1.7-x}ON_{1.8}$ anode does not involve the alloying and conversion reaction. The similar CV curves of the $GeZn_{1.7-x}ON_{1.8}$ and pristine $GeZn_{1.7}ON_{1.8}$ anodes reveal that the Zn vacancy shows limited influence on the lithiation mechanism. As shown in Fig. 4b, the $GeZn_{1.7-x}ON_{1.8}$ particle anode shows typical charge/discharge curves with high reversibility. The galvanostatic charge/discharge profiles demonstrate that the initial discharge and charge capacities are 988.4 and 889.2 mA h g^{-1}, respectively, with the initial coulombic efficiency of 89.9%. The initial irreversible capacity loss might result from the SEI layer and electrolyte decomposition, which leads to irreversible capacity loss.[46] With the increase in the cycle number, the coulombic efficiency increases gradually and maintains 100% after 12 cycles. The overlapped cycle curves imply the excellent stability of the electrochemical reaction. In the following cycles, the overlapping discharge/charge profiles imply the good structural stability and reversible electrochemical reaction, matching well with the CV results. As shown in Fig. 4c, the reversible capacity gradually decreases in the first 30 cycles and maintains a highly stable reversible capacity in the subsequent cycles. This phenomenon can be associated with the lithiation-induced reactivation process, which is commonly found in the nanostructure-based electrodes.[47] After experiencing a quick activation process in the initial 30 cycles, the discharge capacity increases gradually. After 200 cycles, the $GeZn_{1.7-x}ON_{1.8}$ particle anode still maintains charge/discharge capacities of 868.1 mA h g^{-1} and 858.5 mA h g^{-1}, with almost 100% coulombic efficiency. For the $GeZn_{1.7}ON_{1.8}$ particle anode, after 200 cycles, the discharge capacity is 412 mA h g^{-1}. Those results indicate the good reversibility of the $GeZn_{1.7-x}ON_{1.8}$ particle anode. Therefore, the improved capacity can be ascribed to the enhanced ion/electron diffusion efficiencies and reduced lithium-ion diffusion barrier after acid etching. Fig. 4d shows the rate performances of both the $GeZn_{1.7-x}ON_{1.8}$ and $GeZn_{1.7}ON_{1.8}$ particle anodes at different current densities. The Co–$GeZn_{1.7}ON_{1.8}$ particle anode delivers reversible capacities of 844.2, 727.7, 561.4, 454.8, 357.5, and 265.7 mA h g^{-1} at 0.1, 0.2, 0.5, 1.0, 2.0, and 4.0 A g^{-1}, respectively. It is clear that the $GeZn_{1.7-x}ON_{1.8}$ particle anode still maintains a good reversible capacity of 189.4 mA h g^{-1} at 5.0 A g^{-1}, indicating the excellent rate capacity. When the current density reverts back to 0.1 A g^{-1}, the capacity can be recovered, showing the good reversibility and stability of the $GeZn_{1.7-x}ON_{1.8}$ particle anode. The charge/discharge curves (Fig. 4e) also reveal the reversibility of the electrochemical reaction at different current densities. The enhanced rate

performance can be attributed to the reduced lithium-ion diffusion barrier and excellent ion diffusion efficiency after acid etching. After 2000 cycles (Fig. 4g), the $GeZn_{1.7-x}ON_{1.8}$ particle anode still shows a stable specific capacity of 458.6 mA h g^{-1} at 1.0 A g^{-1}, and its capacity retention ratio is about 76.8% (Fig. 4f). The specific capacity of $GeZn_{1.7}ON_{1.8}$ particle anode is only about 156 mA h g^{-1}, and its capacity retention ratio is approximately 42.5%. This result indicates that the $GeZn_{1.7-x}ON_{1.8}$ particle anode can maintain high cyclic stability under high current density conditions.

The CV curves in Fig. 5a show a similar shape at different scan rates, indicating the negligible polarization of the electrochemical reaction.[48] Based on $i = av^b$ (where i and v are the current density and scan rate, respectively), the calculated b values ($0.5 \leq b \leq 1$) reveal the coexistence of the capacitive and diffusive contributions during the charge/discharge processes.[49] The pseudo-capacitance contribution can be determined precisely by capacitive effects (k_1v) and diffusion-controlled insertion ($k_2v^{1/2}$). As shown in Fig. 5b, more than 70% of the total lithium-ion storage comes from the capacitive process at 1.0 mV s^{-1}, and the charge diffusion process is mainly concentrated at low-voltage regions (≤0.5 V).[50] As shown in Fig. 5c, the contribution of the pseudo-capacitance progressively increases and diffusion contribution decreases with the increase in the scan rate, and this result is in good agreement with the previous report.[51] Galvanostatic intermittent titration technique (GITT) analysis was further performed to analyze the charge transfer behavior of the $GeZn_{1.7-x}ON_{1.8}$ particle anode. As shown in Fig. 5d, the negligible overpotential indicates the fast charge transfer efficiency and stable reaction resistance during the electrochemical reaction.[52] Compared with the $GeZn_{1.7}ON_{1.8}$ particle anode, the $GeZn_{1.7-x}ON_{1.8}$ particle anode exhibits a higher capacity and lower reaction resistance, indicating its improved lithium-ion diffusion kinetics. Based on Fick's second law (Fig. 5e), the lithium-ion diffusion coefficient (D_{Li}^{+}) can be determined from the linear relationship between the voltage and square root of the pulse duration ($\tau^{1/2}$). As shown in Fig. 5f, a similar overall trend of D_{Li}^{+} manifests the same lithium-ion diffusion behavior and electrochemical reaction mechanism, and the higher lithium-ion diffusion coefficient means the higher charge transfer kinetics. The stable ion diffusion process reveals that no conversion and alloying reactions occur in the charge/discharge processes.[53] The *in situ* response resistance was further calculated based on the closed-circuit voltage and the quasi-open circuit voltage. As shown in Fig. 5g, the reaction resistance of

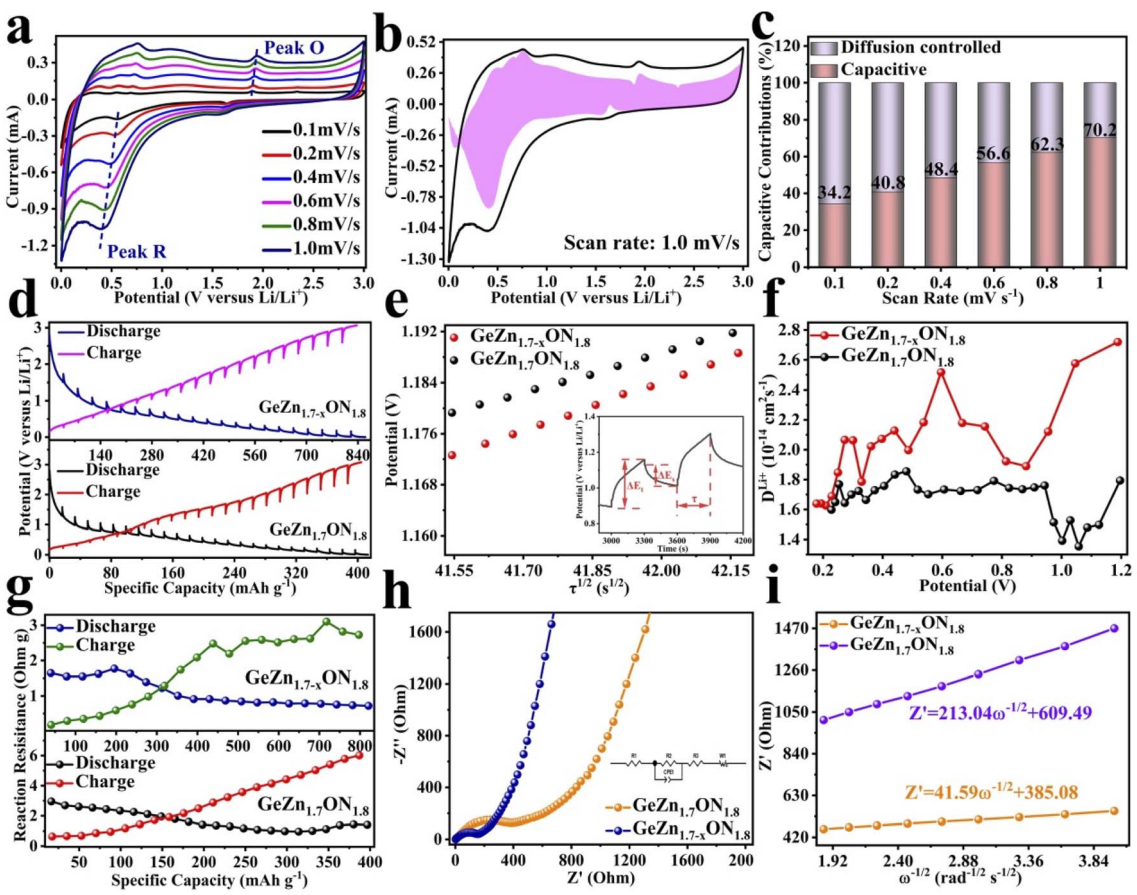

Fig. 5 Kinetic analysis of $GeZn_{1.7-x}ON_{1.8}$: (a) CVs curves from 0.1 to 1.0 mV s^{-1}. (b) Pseudocapacitive contribution shown by pink region at 1.0 mV s^{-1}. (c) Pseudocapacitive contribution ratio from 0.1 to 1.0 mV s^{-1}. (d) Potential response in the GITT profiles. (e) Relationship between potential and $\tau^{1/2}$ (inset: titration profile). (f) Lithium-ion diffusion coefficients and (g) reaction resistances calculated by GITT profiles. (h) Nyquist plots and (i) relationship between Z' and $\omega^{-1/2}$.

the $GeZn_{1.7-x}ON_{1.8}$ particle anode is lower, indicating the improved conductivity and lithium-ion diffusion kinetics after acid etching. Electrochemical impedance spectroscopy (EIS) analysis was performed to further investigate the lithium-ion diffusion behavior. As shown in Fig. 5h, the semicircles in the high-to-medium frequency region represent the charge-transfer resistance (R_{ct}) and impedance of the SEI layer (R_{SEI}), and the inclined line in the low-frequency region represents the mass-transfer resistances (Warburg impedance, R_w).[54] After the equivalent circuit model fitting (inset in Fig. 5h), the R_{ct} value of the $GeZn_{1.7-x}ON_{1.8}$ particle anode (162.4 Ω) is smaller than that of the $GeZn_{1.7}ON_{1.8}$ (345.3 Ω) particle anode, indicating the high electrical conductivity of acid etching. In the inclined region, the higher slope manifests better lithium-ion mobility. According to $Z_{real} = R_e + R_{ct} + \sigma\omega^{-1/2}$, in Fig. 5i, the calculated Warburg factor (σ) of the $GeZn_{1.7-x}ON_{1.8}$ particle (41.59) is much lower than that of the $GeZn_{1.7}ON_{1.8}$ particle (213.04), and the calculated D_{Li}^{+} values of the $GeZn_{1.7}ON_{1.8}$ and $GeZn_{1.7-x}ON_{1.8}$ particle anodes are 1.78×10^{-14} and 2.36×10^{-14} $cm^2 s^{-1}$, respectively. These results indicate the enhanced lithium-ions diffusion efficiency after acid etching.

To better understand the lithium-ion storage mechanism, XRD and XPS analyses were performed in different electrochemical states (Fig. 6a). As shown in Fig. 6b and c, the diffraction peaks at 43.3° and 50.4° (marked with asterisk) come from the copper foil. The diffraction peaks of $GeZn_{1.7-x}ON_{1.8}$ are observed in the whole electrochemical reaction, and no additional diffraction peaks about Ge or Zn appear, showing the reversible lithium-ion storage mechanism and good structural stability. To further analyze the structural changes, the XRD

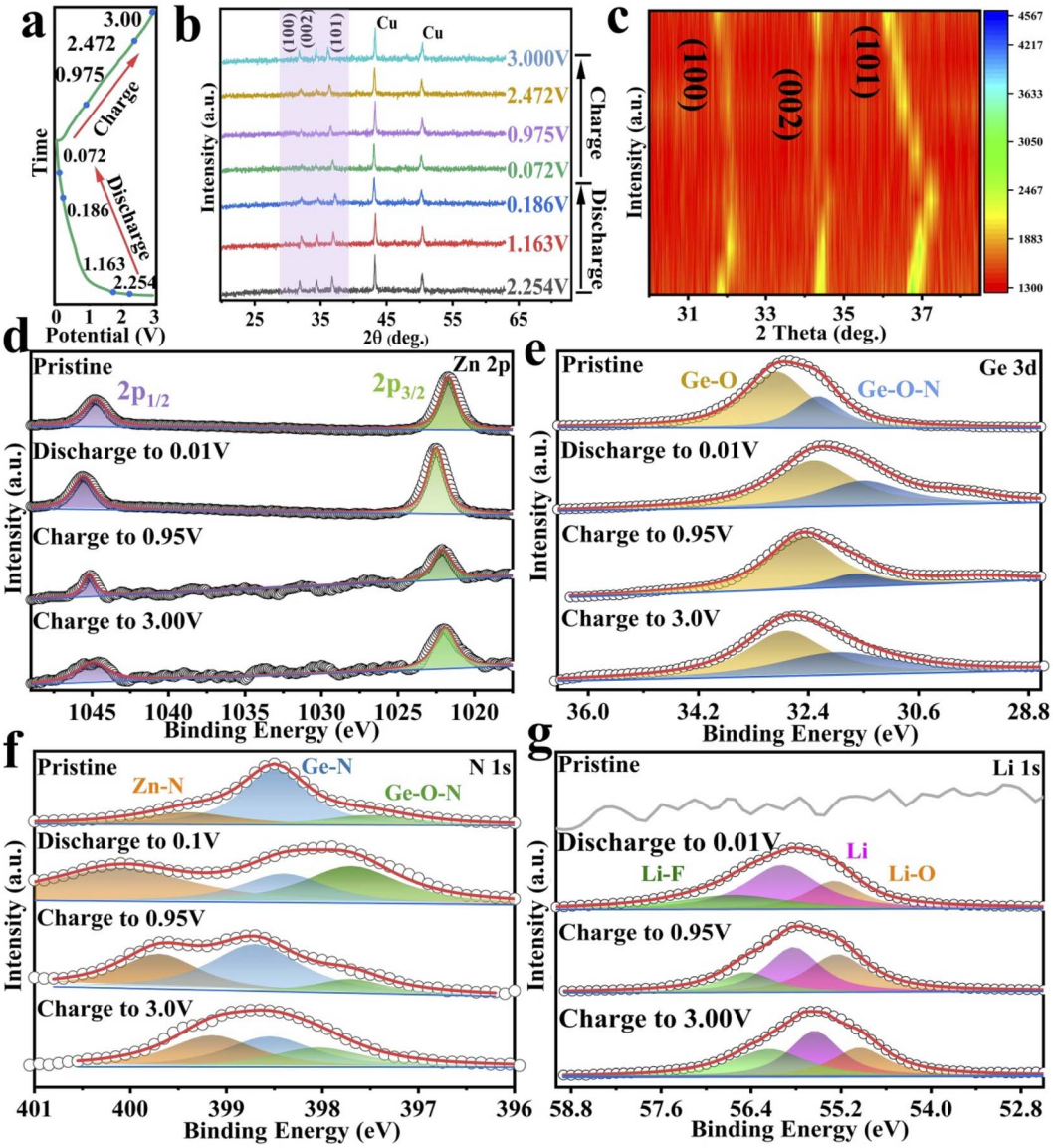

Fig. 6 Lithium-ion storage mechanism study of the $GeZn_{1.7-x}ON_{1.8}$ particle anode. (a) Charge/discharge profile and the corresponding (b) XRD patterns. The shallow region represents (c) the intensity contour map of characteristic diffraction peaks from 30° to 40°. (d)–(g) XPS analysis of the $GeZn_{1.7-x}ON_{1.8}$ particle anode at different charge/discharge states.

profiles are expanded in the form of intensity isopleth maps in the characteristic peak region (from 30° to 40°), as shown in Fig. 6c. In the discharged states, the characteristic diffraction peaks (at 32.3°, 34.5°, and 36.7°) shift toward a higher angle direction as the diffraction intensity is decreased, and the characteristic diffraction peaks are gradually broadened with the lattice expansion, revealing the reversible lithium-ion storage mechanism. The decreased diffraction intensity of the characteristic peaks may be due to the reduced crystallinity after lithium-ion insertion.[55] In the charge states, the characteristic peaks shift toward the opposite direction with the lithium-ion desertion reaction. The XRD analysis clearly shows reversible lithium-ion storage mechanism of the $GeZn_{1.7-x}ON_{1.8}$ particles.

The electrochemical charge storage mechanism was further confirmed by XPS analysis in different electrochemical states. For the Zn 2p spectrum before discharge (Fig. 6d), the main peaks at 1022.5 and 1045.7 eV correspond to Zn $2p_{3/2}$ and Zn $2p_{1/2}$.[56] At the complete discharge state (0.01 V), the Zn $2p_{3/2}$ and Zn $2p_{1/2}$ peaks move to 1023.4 and 1046.5 eV, respectively, indicating similar bonding conditions during the discharge.[36] In addition, in the fully discharged state, the electronic states of Zn $2P_{3/2}$ and Zn $2P_{1/2}$ are significantly different from metal Zn^0, which reveals the reversible lithium-ion storage mechanism of $GeZn_{1.7-x}ON_{1.8}$ particles.[57] The Ge 3d spectrum (Fig. 6e) shows that the Ge–O and Ge–O–N core energy levels of pristine $GeZn_{1.7-x}ON_{1.8}$ are located at 32.8 and 32.2 eV, respectively.[38,39] During the discharge process, the Ge 3d spectrum shifts to a lower energy, while the Ge 3d spectrum shifts to a higher energy during the charging process. Compared with the pristine state, the lower binding energy shift of the fully charged Ge 3d spectrum is attributable to the existence of lithium-ions in the interlayers and on the surface of the anode and also due to the SEI film formation.[58] This periodical change in the Ge 3d spectrum also reveals the reversible lithium-ion storage mechanism of the $GeZn_{1.7-x}ON_{1.8}$ particle. Moreover, the high-resolution N 1s spectra at different charging/discharging states were further analyzed (Fig. 6f). Before discharge, the major peaks at 399.6, 398.3, and 397.6 eV could be assigned to Zn–N, Ge–N, and Ge–O–N bonds, respectively.[36] During discharge, the N 1s spectrum shifts toward higher energies, while during charging, the N 1s spectrum shifts toward lower energies. The binding energy shift of the fully charged N 1s spectrum is higher than that of the pristine state. The N 1s spectrum with minor intensity changes in the coordination further confirms that the lithium-ion storage mechanism involves lithiation/delithiation reactions. The peak at 55.5 eV could be attributed to lithium alkyl carbonate in the discharge product as shown in the Li 1s spectrum (Fig. 6g).[59] The Li–O bond at 54.8 eV could be attributed mainly to the oxidizing electrolyte in air. The Li–F bond (56.6 eV) exists in the overall lithiation/delithiation processes.[60,61] Based on all the analyses, the overall reaction mechanism of the $GeZn_{1.7-x}ON_{1.8}$ particle anode during the lithiation/delithiation processes can be expressed as eqn (1):

$$GeZn_{1.7-x}ON_{1.8} + xLi^+ + xe^- \leftrightarrow Li_xGeZn_{1.7-x}ON_{1.8} \quad (1)$$

4. Conclusion

In summary, $GeZn_{1.7-x}ON_{1.8}$ particles have been successfully prepared by an ammoniation and acid etching method as confirmed by XRD, EDS, EPR, and XPS characterization techniques. The Mott–Schottky testing demonstrated an efficient electron transport in $GeZn_{1.7-x}ON_{1.8}$ particle anodes. Systematic electrochemical analyses revealed that the $GeZn_{1.7-x}ON_{1.8}$ particle anode possessed a higher rate capacity and excellent cyclic stability compared with the pristine $GeZn_{1.7}ON_{1.8}$ particle anode. Electrochemical kinetics analysis further proved the excellent electrochemical behavior of the $GeZn_{1.7-x}ON_{1.8}$ particle anodes. Furthermore, the XRD and XPS results obtained at different electrochemical reaction states show that the good cyclic stability could be attributed to favorable structural tolerance and reversible lithium-ion storage mechanism. This study provides a feasible way to understand high-performance quaternary metal oxynitride anodes prepared *via* rational design defect engineering.

Conflicts of interest

The authors declare no conflict of interest.

Acknowledgements

This work was supported by the Foundation of Chinese Academy of Sciences Science and Technology Service Network Program-Dongguan Special Project (No. 2137003); the High-level Talents (GB200902-30, No. 196100041018 and GB 200902-43, No. 196100041009), the Foundation of Regular Research Team (TDYB2019007, No. 196100043028 and No. 2062011047), the Foundation of Young Research Team (TDQN2019004, No. 193500008008) at Dongguan University of Technology, the Guangdong Basic and Applied Basic Research Foundation (2019A1515110933, 2019A1515110554, 2020A1515111086, 2020A1515110219, and 2020A1515110770), China Postdoctoral Science Foundation (Grant No. 2021M700915), and the Foundation of Doctor's Workstation of Mcnair New Power Co., Ltd (GC200104-40, No. 186100030017).

References

1 J. Ni, Y. Zhao, L. Li and L. Mai, *Nano Energy*, 2015, **11**, 129–135.
2 J. R. Rodriguez, Z. Qi, H. Wang, M. Y. Shalaginov, C. Goncalves, M. Kang, K. A. Richardson, J. Guerrero-Sanchez, M. G. Moreno-Armenta and V. G. Pol, *Nano Energy*, 2020, **68**, 104326.
3 W. Li, X. Li, J. Yu, J. Liao, B. Zhao, L. Huang, A. Ali, H. Zhang, J. H. Wang, Z. Guo and M. Liu, *Nano Energy*, 2019, **61**, 594–603.
4 C. Sun, Y.-J. Wang, H. Gu, H. Fan, G. Yang, A. Ignaszak, X. Tang, D. Liu and J. Zhang, *Nano Energy*, 2020, **77**, 105092.
5 T. Wang, C. Sun, M. Yang, L. Zhang, Y. Shao, Y. Wu and X. Hao, *Electrochim. Acta*, 2018, **259**, 1–8.

6 T. Wang, J. Shen, M. Yang, C. Cheng, Y. Zhang, C. Sun and L. Zhang, *Ceram. Int.*, 2021, **47**, 21610.
7 T. Wang, C. Sun, M. Yang, G. Zhao, S. Wang, F. Ma, L. Zhang, Y. Shao, Y. Wu, B. Huang and X. Hao, *J. Alloys Compd.*, 2017, **716**, 112–118.
8 C. Sun, X. Tang, Z. Yin, D. Liu, Y.-J. Wang, G. Yang, A. Ignaszak and J. Zhang, *Nano Energy*, 2020, **68**, 104376.
9 C. Sun, M. Yang, T. Wang, Y. Shao, Y. Wu and X. Hao, *ACS Appl. Mater. Interfaces*, 2017, **9**, 26631–26636.
10 C. Sun, M. Yang, T. Wang, Y. Shao, Y. Wu and X. Hao, *ACS Appl. Mater. Interfaces*, 2018, **10**, 2574–2580.
11 T. Wang, G. Zhao, C. Sun, L. Zhang, Y. Wu, X. Hao and Y. Shao, *Adv. Mater. Interfaces*, 2017, **4**, 1601187.
12 M. Yang, C. Sun, T. Wang, F. Chen, M. Sun, L. Zhang, Y. Shao, Y. Wu and X. Hao, *ACS Appl. Energy Mater.*, 2018, **1**, 4708–4715.
13 W. H. Choi, C. H. Lee, H.-e. Kim, S. U. Lee and J. H. Bang, *Nano Energy*, 2020, **74**, 104829.
14 B. Long, H. Yang, F. Wang, Y. Mao, M.-S. Balogun, S. Song and Y. Tong, *Electrochim. Acta*, 2018, **284**, 271–278.
15 B. Zou, W. Zhang, Y. Cui, S. Li, G. Li, X. Liu, D. H. L. Ng, J. Qiu and J. Lian, *J. Mater. Chem. A*, 2022, **10**, 7391–7398.
16 B. Long, M.-S. Balogun, L. Luo, Y. Luo, W. Qiu, S. Song, L. Zhang and Y. Tong, *Small*, 2017, **13**, 1702081.
17 K. Xie, J. Wang, S. Yu, P. Wang and C. Sun, *Arabian J. Chem.*, 2021, **14**, 103161.
18 A. Achour, J. B. Ducros, R. L. Porto, M. Boujtita, E. Gautron, L. Le Brizoual, M. A. Djouadi and T. Brousse, *Nano Energy*, 2014, **7**, 104–113.
19 X. Yang, X. Li, K. Adair, H. Zhang and X. Sun, *Electrochem. Energy Rev.*, 2018, **1**, 239–293.
20 L. Bai, Y. Zhang, W. Tong, L. Sun, H. Huang, Q. An, N. Tian and P. K. Chu, *Electrochem. Energy Rev.*, 2020, **3**, 395–430.
21 C. Sun, F. Chen, X. Tang, D. Zhang, K. Zheng, G. Zhu, U. Bin Shahid, Z. Liu, M. Shao and J. Wang, *Nano Energy*, 2022, **99**, 107369.
22 W. Cha, S. Kim, P. Selvarajan, J. M. Lee, J. M. Davidraj, S. Joseph, K. Ramadass, I. Y. Kim and A. Vinu, *Nano Energy*, 2021, **82**, 105733.
23 S. Wang, C. Sun, Y. Shao, Y. Wu, L. Zhang and X. Hao, *Small*, 2017, **13**, 1603330.
24 Y. Wu, P. Lazic, G. Hautier, K. Persson and G. Ceder, *Energy Environ. Sci.*, 2013, **6**, 157–168.
25 C. Sun, F. Ma, L. Cai, A. Wang, Y. Wu, M. Zhao, W. Yan and X. Hao, *Sci. Rep.*, 2017, **7**, 6617.
26 Z. Li, K. Gao, Y. Han, S. Ding, Y. Cui, M. Hu, J. Zhao, M. Zhang, A. Meng, J. Yun, Z. Liu, D.-W. Wang and C. Sun, *J. Energy Chem.*, 2022, **67**, 46–54.
27 G. Ali, J.-H. Lee, S. H. Oh, H.-G. Jung and K. Y. Chung, *Nano Energy*, 2017, **42**, 106–114.
28 H. He, D. Huang, Y. Tang, Q. Wang, X. Ji, H. Wang and Z. Guo, *Nano Energy*, 2019, **57**, 728–736.
29 G. Huang, Y. Yang, H. Sun, S. Xu, J. Wang, M. Ahmad and Z. Xu, *J. Alloys Compd.*, 2017, **724**, 1149–1156.
30 C. Schliehe and C. Giordano, *Nanoscale*, 2013, **5**, 3235–3239.
31 L. Pan, S. Wang, W. Mi, J. Song, J.-J. Zou, L. Wang and X. Zhang, *Nano Energy*, 2014, **9**, 71–79.
32 S. Li, Y. Xiao, X. Wang and M. Cao, *Phys. Chem. Chem. Phys.*, 2014, **16**, 25846–25853.
33 L. Huang, G. H. Waller, Y. Ding, D. Chen, D. Ding, P. Xi, Z. L. Wang and M. Liu, *Nano Energy*, 2015, **11**, 64–70.
34 Y. Xu, M. Zhou, C. Zhang, C. Wang, L. Liang, Y. Fang, M. Wu, L. Cheng and Y. Lei, *Nano Energy*, 2017, **38**, 304–312.
35 X. Jiao, Z. Chen, X. Li, Y. Sun, S. Gao, W. Yan, C. Wang, Q. Zhang, Y. Lin, Y. Luo and Y. Xie, *J. Am. Chem. Soc.*, 2017, **139**, 7586–7594.
36 Y. Han, C. Sun, K. Gao, S. Ding, Z. Miao, J. Zhao, Z. Yang, P. Wu, J. Huang, Z. Li, A. Meng, L. Zhang and P. Chen, *Electrochim. Acta*, 2022, **408**, 139931.
37 D. Choi, G. E. Blomgren and P. N. Kumta, *Adv. Mater.*, 2006, **18**, 1178–1182.
38 Y. Zhu, N. Jain, M. K. Hudait, D. Maurya, R. Varghese and S. Priya, *J. Vac. Sci. Technol., B: Nanotechnol. Microelectron.: Mater., Process., Meas., Phenom.*, 2014, **32**, 011217.
39 K. S. Agrawal, V. S. Patil, A. G. Khairnar and A. M. Mahajan, *Appl. Surf. Sci.*, 2016, **364**, 747–751.
40 A. B. Djurišić, W. C. H. Choy, V. A. L. Roy, Y. H. Leung, C. Y. Kwong, K. W. Cheah, T. K. Gundu Rao, W. K. Chan, H. Fei Lui and C. Surya, *Adv. Funct. Mater.*, 2004, **14**, 856–864.
41 Z. Ma, O. Linnenberg, A. Rokicinska, P. Kustrowski and A. Slabon, *J. Phys. Chem. C*, 2018, **122**, 19281–19288.
42 M. M. Rahman, I. Sultana, T. Yang, Z. Chen, N. Sharma, A. M. Glushenkov and Y. Chen, *Angew. Chem., Int. Ed.*, 2016, **128**, 16293–16297.
43 Q. Peng, Y. Lei, Z. Tang, C. Sun, J. Li, G. Wu, T. Wang, Z. Yin and H. Liu, *Electrochim. Acta*, 2020, **350**, 136380.
44 K. Zhang, H. Wang, X. He, Z. Liu, L. Wang, L. Gu, H. Xu, P. Han, S. Dong and C. Zhang, *J. Mater. Chem.*, 2011, **21**, 11916–11922.
45 Y. Wu, L. Huang, X. Huang, X. Guo, D. Liu, D. Zheng, X. Zhang, R. Ren, D. Qu and J. Chen, *Energy Environ. Sci.*, 2017, **10**, 1854–1861.
46 D. Kundu, F. Krumeich, R. Fotedar and R. Nesper, *J. Power Sources*, 2015, **278**, 608–613.
47 C. Yan, C. Lv, Y. Zhu, G. Chen, J. Sun and G. Yu, *Adv. Mater.*, 2017, **29**, 1703909.
48 X. Xia, D. Chao, Y. Zhang, J. Zhan, Y. Zhong, X. Wang, Y. Wang, Z. X. Shen, J. Tu and H. J. Fan, *Small*, 2016, **12**, 3048–3058.
49 P. He, Y. Quan, X. Xu, M. Yan, W. Yang, Q. An, L. He and L. Mai, *Small*, 2017, **13**, 1702551.
50 C. Chen, Y. Wen, X. Hu, X. Ji, M. Yan, L. Mai, P. Hu, B. Shan and Y. Huang, *Nat. Commun.*, 2015, **6**, 6929.
51 G. Fu, Z. Cui, Y. Chen, L. Xu, Y. Tang and J. B. Goodenough, *Nano Energy*, 2017, **39**, 77–85.
52 J. Zhou, Z. Jiang, S. Niu, S. Zhu, J. Zhou, Y. Zhu, J. Liang, D. Han, K. Xu, L. Zhu, X. Liu, G. Wang and Y. Qian, *Chem*, 2018, **4**, 372–385.
53 S. Wang, S. Liu, X. Li, C. Li, R. Zang, Z. Man, Y. Wu, P. Li and G. Wang, *Chem.–Eur. J.*, 2018, **24**, 3873–3881.
54 S. S. Zhang, *J. Electrochem. Soc.*, 2012, **159**, A920–A923.
55 X. Xu, C. Niu, M. Duan, X. Wang, L. Huang, J. Wang, L. Pu, W. Ren, C. Shi, J. Meng, B. Song and L. Mai, *Nat. Commun.*, 2017, **8**, 460.

56 J. Chu, W. A. Wang, J. Feng, C.-Y. Lao, K. Xi, L. Xing, K. Han, Q. Li, L. Song, P. Li, X. Li and Y. Bao, *ACS Nano*, 2019, **13**, 6906–6916.
57 F. Yang, P. Song, X. Liu, B. Mei, W. Xing, Z. Jiang, L. Gu and W. Xu, *Angew. Chem., Int. Ed.*, 2018, **57**, 12303–12307.
58 F. W. Fenta, B. W. Olbasa, M.-C. Tsai, M. A. Weret, T. A. Zegeye, C.-J. Huang, W.-H. Huang, T. S. Zeleke, N. A. Sahalie, C.-W. Pao, S.-h. Wu, W.-N. Su, H. Dai and B. J. Hwang, *J. Mater. Chem. A*, 2020, **8**, 17595–17607.
59 E. Radvanyi, W. Porcher, E. De Vito, A. Montani, S. Franger and S. J. S. Larbi, *Phys. Chem. Chem. Phys.*, 2014, **16**, 17142–17153.
60 P. Guan, L. Liu and X. Lin, *J. Electrochem. Soc.*, 2015, **162**, A1798–A1808.
61 R. Younesi, P. Norby and T. Vegge, *ECS Electrochem. Lett.*, 2014, **3**, A15–A18.